Nonlinear control and stability analysis of a stroke limited inertial actuator in velocity feedback

Mattia Dal Borgo[*], Maryam Ghandchi Tehrani[*] and Stephen John Elliott [*]
[*]*Institute of Sound and Vibration Research, University of Southampton, Southampton, UK*

Summary. Inertial actuators are active devices used, with velocity feedback controllers, to reduce structural vibrations. Physical limits, such as stroke saturation, can affect the behaviour and the stability of the control system. In particular, limit cycle oscillations are observed. In this paper, we propose a nonlinear control strategy to prevent the destabilisation of the velocity feedback loop due to stroke saturation. A time domain model of the stroke limited inertial actuator mounted on a single degree of freedom structure is derived. The stability of the nonlinear system under a velocity feedback control with fixed gain is investigated using the describing function method for the detection of limit cycles. The outcomes are also verified by time domain simulations. The presented nonlinear controller increases the stability region of the system compared to only the velocity feedback controller.

Introduction

Extensive research has shown the importance of active devices to control vibrations of lightweight and flexible structures [1-7]. The use of electromagnetic inertial, or proof mass, actuators as active forcing devices in velocity feedback controllers has also been well documented [2, 5, 7-13]. A velocity feedback controller consists of an electromagnetic actuator attached to a structure, a collocated sensor of vibration (usually an accelerometer) and a controller, which feeds back the velocity of the structure to the actuator. In fact, velocity feedback controllers are capable to add a certain quantity of viscous damping into the structure reducing its level of vibration in particular in the region of its resonances. An inertial actuator consists of a magnetic proof mass, an electrical winding and a suspension, which connects the proof mass to a casing. The way an inertial actuator operates is using an input current to generate the control force on the structure and reacting against the proof mass, which starts to accelerate [7]. The main concern using inertial actuators in a velocity feedback loop is that they are only conditionally stable [14], hence there exists a maximum feedback gain, over which the system becomes unstable. [8, 15-25]. Most studies in this area have not dealt with nonlinear models of actuators, limiting them to work in restricted operating conditions. The most important nonlinearity encountered by the authors that can affect the dynamic behaviour of an inertial actuator is a saturation phenomenon of the force that can be delivered. The limitation of the force generated by the actuator can be due to a saturation of the power electronics. Also, it can be due to the finite stroke length between the end stops within the actuator casing, for a certain value of the proof mass. Figure 1(a) shows a simple model of a proof mass actuator blocked at the base, which can be used to demonstrate the limitation of the linear analysis. According to Newton's second law, the equation of motion of the proof mass can be written as,

$$m_p\ddot{x}_p + c_p\dot{x}_p + k_p x_p = (Bl)i_a \tag{1}$$

where m_p is the proof mass of the inertial actuator, c_p and k_p are the linear damping and stiffness associated with the proof mass suspension, respectively. The variable i_a denotes the current flowing through the coil, B is the magnetic field generated by the permanent magnet and l is the length of the winding exposed to the magnetic flux density B. The displacement of the proof mass with respect to its equilibrium position is named x_p. The force acting on the ground, namely blocked force f_b, provided by the inertial actuator results in,

$$f_b = k_p x_p + c_p\dot{x}_p - (Bl)i_a \tag{2}$$

according to the sign convention of Figure 1(a). Combining equations (1) and (2), the blocked force can also be written as,

$$f_b = -m_p\ddot{x}_p \tag{3}$$

Applying Laplace transform to both equations (2) and (3) and considering harmonic motion ($s = j\omega$), after a few mathematical manipulations, the maximum blocked force that the actuator can deliver $F_{b,max}(j\omega)$, as described by the linear analysis, is given by

$$F_{b,max}(j\omega) = \begin{cases} F_{b,max1}(j\omega) = F_{a,max}(j\omega)\left(\dfrac{(\omega/\omega_p)^2}{-(\omega/\omega_p)^2 + 2j\zeta_p(\omega/\omega_p) + 1}\right) \\ F_{b,max2}(j\omega) = m_p\omega^2 x_0 \end{cases} \tag{4}$$

where $F_{b,max1}(j\omega)$ and $F_{b,max2}(j\omega)$ represent the force saturation due to the power electronic saturation and the stroke saturation respectively. Also, the natural frequency of the inertial actuator is defined as $\omega_p = \sqrt{k_p/m_p}$, and the damping ratio as $\zeta_p = c_p/(2m_p\omega_p)$. The power electronic saturation gives a limitation on the electromechanical conversion, which is given by the maximum actuation force $F_{a,max}(j\omega)$ as,

$$F_{a,max}(j\omega) = (Bl)I_{a,max}(j\omega) \tag{5}$$

where $I_{a,max}(j\omega)$ is the maximum input current to the actuator coil. The stroke saturation gives a limitation on the maximum displacement achievable for the proof mass. This is given by,

$$X_{p,max}(j\omega) = x_0 \tag{6}$$

where x_0 is half of the stroke length. The results of this analysis are shown in Figure 1(b) for a Micromega Dynamics IA-01 inertial actuator, whose parameters are given in [26]. The dotted and dash-dotted blue lines in Figure 1(b) show in a logarithmic scale the spectrum of the actuation force $F_{a,max}(j\omega)$ and the blocked force $F_{b,max1}(j\omega)$, when the actuator is driven by maximum current. The dashed red line shows instead the spectrum of the blocked force $F_{b,max2}(j\omega)$, when the actuator is driven at the maximum stroke of the proof mass.

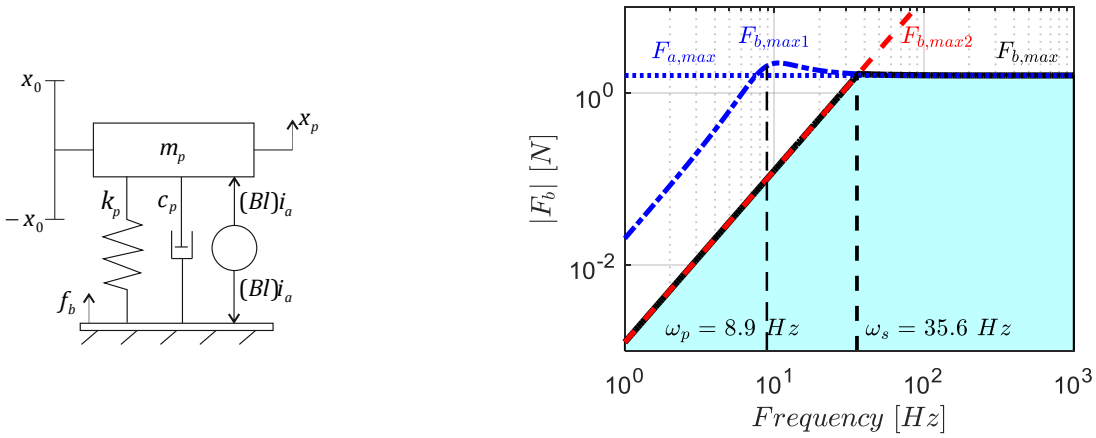

(a) (b)

Figure 1. (a) Schematic of the mechanical model for the grounded proof mass actuator; (b) Limitation of the linear analysis for a proof mass actuator. Dotted and dash-dotted blue lines represent the limitation on the maximum force due to saturation of the power electronics; red dashed line displays the limitation due to the maximum stroke available; black solid line is the combination of the two previous constraints and gives a limit on the region of linear operation of the inertial actuator (cyan area).

A combination of these two limitations results in a region of linear operation for the inertial actuator, which is delimited upwards by the black solid line. The upper limit for the input current, whose dynamics are flat over the frequency range, is indeed a limitation on the temperature and heating of the actuator. As it is well described in [15, 16], an increase in the input power to the actuator's coil would produce a temperature rise of its components. The maximum current is given by the maximum temperature rise, which does not lead to demagnetisation of the proof mass caused by passing the Curie temperature (for most of permanent magnets is about 80 °C), when the atoms of the material deviate from the magnetic alignment. An ultimate limit is then given by the melting temperature of the wire insulation, which is about 150 °C for common materials [16]. The force limit due to stroke saturation shown in Figure 1(b) appears to be an effective limit at low frequencies, instead. The plot of Figure 1(b) can thus be divided in two regions: below the saturation cut off frequency ω_s, where the limitation of the blocked force is given by stroke saturation; and above the saturation cut off frequency, where the limit is given by the power electronics. In this paper, we focus our attention onto the nonlinearity due to the stroke limits. The displacement saturation phenomenon in inertial actuators has been investigated in [8, 17, 23, 24, 27-29]. Indeed the implication of stroke saturation is not the only limitation on the amount of force available from the actuator. If the proof mass is driven against its end stops, hence saturating in the displacement, large shocks are imparted to the actuator casing and to the structure, and damage may result. Moreover, this phenomenon is undesirable in terms of the stability of the closed loop control system, because it can reduce the stability margin of the velocity feedback loop, and in fact, enhance the level of vibration [17]. It has also been observed experimentally that this problem affects systems with multiple actuators and local velocity controllers [14]. In this case, the instability in one loop leads to instability in all the other loops [14]. Hence, the dynamic behaviour of inertial actuators is not always well described by a linear mathematical model [8, 15-25].

This paper analyses the impact of a previously identified nonlinear model of an inertial actuator [25] on the stability of the velocity feedback control loop, and proposes a nonlinear feedback controller, which is able to increase the safe operating region of the actuator. Firstly, the nonlinear behaviour of the inertial actuator is investigated. Secondly, a mathematical model of the nonlinear proof mass actuator attached to a single degree of freedom structure is derived. Then, the stability of the nonlinear system is analysed using the describing function method for the detection of limit cycles. Also, time domain simulations are carried out under different scenarios. Finally, a nonlinear feedback control law is presented, aiming to prevent the instability of the system caused by stroke saturation.

System model

In order to understand the dynamic behaviour of an inertial actuator accounting for stroke saturation, a lumped parameter model is considered, as shown in Figure 2(a), where the actuator is mounted on a rigid structure. The dynamics of the proof mass actuator can be defined as a single degree of freedom (SDoF) oscillator plus a force generator acting between the inertial mass and the actuator casing. The equation of motion is given by,

$$m_p\ddot{x}_p + c_p\dot{x}_p + f_{RF}(x_p) = (Bl)i_a \tag{7}$$

where $f_{RF}(x_p)$ represents the nonlinear restoring force of the system, since the stiffness varies depending on the value of the displacement x_p. The impact, or end stop, stiffness is given by the parameter k_c. All these parameters were identified in a previous experimental work [25]. In this study, the stroke saturation phenomenon has been modelled as an elastic collision between the proof mass and the actuator casing in both directions, assuming an equilibrium position of the proof mass centred within the two end stops. In this way, the model can be seen as a linear SDoF system for displacements lower than the stroke length, and as a nonlinear system with a hardening stiffness, when stroke saturation occurs. Considering the model of Figure 2(a), the overall stiffness for displacements exceeding the stroke length is $k_{sat} = k_c + k_p$. In general, the restoring force for such a model can be written as,

$$f_{RF}(x_p) = \begin{cases} k_{sat}(x_p - x_0) + k_p x_0 & x_p > x_0 \\ k_p x_p & |x_p| \le x_0 \\ k_{sat}(x_p + x_0) - k_p x_0 & x_p < x_0 \end{cases} \tag{8}$$

Equation (8) is also represented in Figure 2(b) for two values of the impact stiffness k_c. Hence, the nonlinearity has been modelled as a symmetric piecewise linear stiffness with a hardening behaviour. It should be noted that if the impact stiffness $k_c = 0$, the system becomes linear.

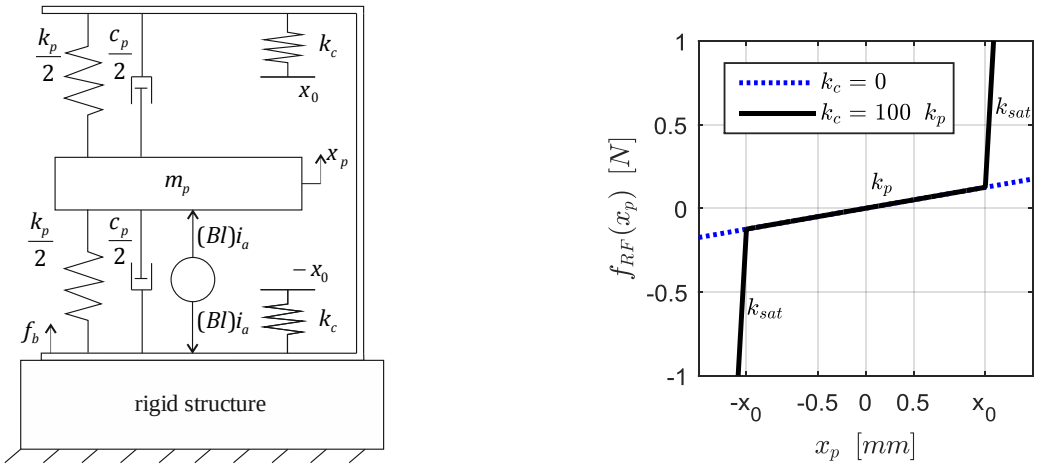

(a) (b)

Figure 2. (a) A lumped parameter model of an inertial actuator with stroke limits; (b) Restoring force plot for the linear actuator (dotted blue line) and the nonlinear actuator (solid black line).

A comparison between the nonlinear actuator with its underlying linear model can be done in frequency domain, using the harmonic balance method (HBM) in order to find the periodic solutions of equation (7). The method is explained in detail by Detroux *et al.* in [30]. Nowadays, HBM has developed to approximate the periodic solution with several harmonics. However, HBM was initially introduced to linearise a nonlinear system with a single harmonic approximation [31]. Hence, the aim of this method is to assume that the response of the nonlinear system to a harmonic excitation is harmonic and at the same frequency of the excitation. The equation of motion (7) is linearised and in particular the restoring force equation (8) is written as,

$$f_{RF}(x_p) \simeq K_{eq}(\omega, X_p)x_p \tag{9}$$

where $K_{eq}(\omega, X_p)$ is an equivalent stiffness for a given operating condition. With this approximation a first-order frequency response function (FRF) for the linearised system between the input phase-shifted excitation $(Bl)i_a(t) = (Bl)i_a \sin(\omega t - \phi)$ and the trial solution $x_p(t) = X_p \sin(\omega t)$ can be obtained,

$$\frac{X_p(j\omega)}{(Bl)I_a(j\omega)} = \Lambda(\omega, X_p) = \frac{1}{K_{eq}(\omega, X_p) + j\omega c_p - m_p\omega^2} \tag{10}$$

where $\Lambda(\omega, X_p)$ denotes the first-order FRF of the nonlinear system, which is also amplitude dependent. Harmonic balance is applied by expanding a Fourier series for equation (8) and imposing the solution $x_p = X_p \sin(\omega t)$. The mathematical derivation of this problem has been addressed in [25] and the final solution for $K_{eq}(\omega, X_p)$ becomes,

$$K_{eq}(X_p) = k_p + \frac{(k_{sat} - k_p)}{\pi}\left[\pi - 2\arcsin\left(\frac{x_0}{X_p}\right) - 2\frac{x_0}{X_p^2}\sqrt{X_p^2 - x_0^2}\right] \tag{11}$$

which is also called the describing function (DF) for the nonlinear stiffness, and it depends on the amplitude of the response X_p. The change of the resonance frequency of the nonlinear system with X_p, with respect to the natural frequency of the underlying linear system, can be obtained from equation (11). The non-dimensional parameter β is considered as,

$$\beta^2 = \frac{\omega_{res,NL}^2}{\omega_p^2} = \frac{K_{eq}(X_p)}{k_p} \tag{12}$$

where $\omega_{res,NL}$ is the resonance frequency of the nonlinear system. An easy interpretation can be established by means of equation (12), which is plotted in Figure 3 for two values of the impact stiffness k_c.

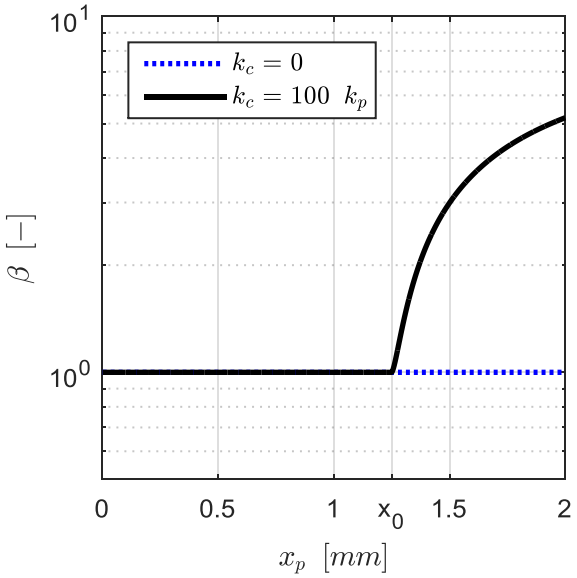

Figure 3. Variation in normalised resonance frequency with excitation level for systems with restoring force as in Figure 2(b).

Indeed, as the response amplitude increases until it reaches the end stop of the inertial actuator, the system is linear with stiffness k_p and $\beta = 1$. If $|X_p|$ is higher than x_0, then a hardened stiffness is encountered and β increases with $|X_p|$. To better understand the nonlinear behaviour of the stroke limited inertial actuator, the computation of higher order nonlinear frequency response curves is required, since the nonsmooth nonlinearity activates higher harmonics. Simulation analysis involving the computation of periodic solutions, which considers higher harmonics is performed using the NI2D® software. The mathematical derivation of the HBM considering higher order periodic solutions can be found in [30, 32]. Figure 4 shows a comparison between the nonlinear frequency response curve (NFRC) obtained computing the periodic solutions up to the 15^{th} harmonic for the nonlinear model of the inertial actuator and the FRF of the underlying linear system, for a frequency range from 2 Hz to 30 Hz and an amplitude excitation of 0.14 N, corresponding to a current $i_a = 0.0875\ A$. It can be observed that the resonance frequency is higher in the nonlinear system than in the underlying linear, as predicted by equation (12) and shown in Figure 3. This is due to the hardening behaviour of the nonlinearity. However, the amplitude of the resonance peak for the nonlinear system is lower than the peak of the underlying linear system. In fact, the nonlinear system is constrained within the stroke limits, which do not permit the proof mass to move any further. This results in the NFRC becoming particularly skewed towards higher frequency with respect to the linear FRF. Figure 5 shows the lumped parameter model of the SDoF structure connected to a nonlinear inertial actuator. The SDoF, also referred to single-input single-output (SISO) system, would represent the first resonance of a real structure. The proof mass m_p is coupled to the structural mass m_s via the actuator suspension parameters $\mathcal{K}(x_r)$ and c_p. Stroke saturation dynamics is, therefore, represented by a piecewise linear stiffness $\mathcal{K}(x_r)$, which is shown by the black solid line of Figure 2(b), where the variable x_p is replaced by x_r. The structural mass is connected to the ground via the stiffness and damping parameters k_s and c_s, respectively. The absolute displacement of the structure is denoted as x_s. Hence, the relative displacement is defined as,

$$x_r = x_p - x_s \tag{13}$$

The structure is subject to the external, or primary, force f_e, and the control, or secondary, force due to the actuator transducer $(Bl)i_a$. L and R are the inductance and resistance associated with the actuator's coil, respectively. The current in the actuator coil and the voltage at its terminals are defined as i_a and e_a, respectively.

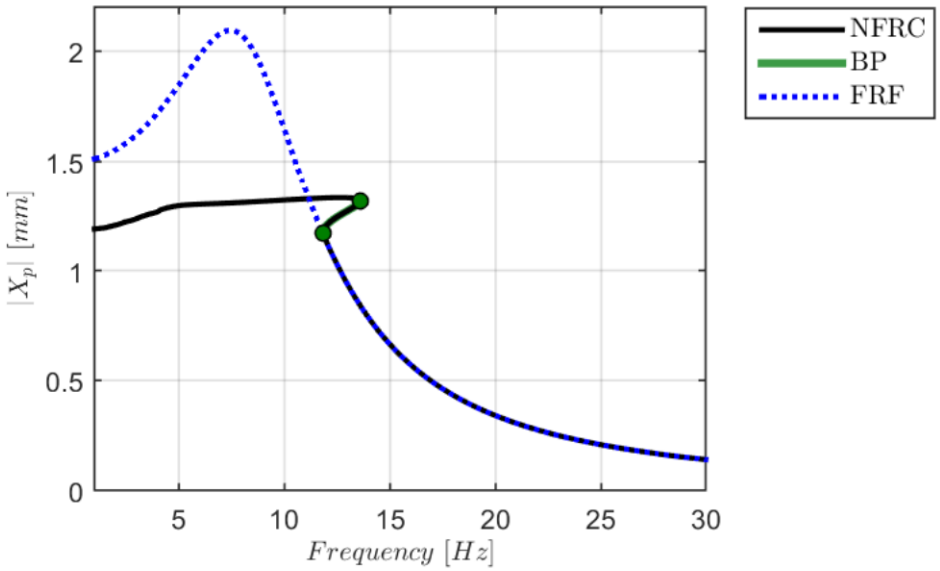

Figure 4. Comparison between linear and nonlinear FRFs. Solid black line represents the nonlinear frequency response curve (NFRC); green circles display the bifurcation points (BP); dotted blue line shows the FRF of the underlying linear system.

The structure's velocity signal $\dot{x}_s$ is multiplied by a fixed gain h_s and fed back to the actuator input current i_a. This forms the linear velocity feedback control loop (VFC). Alongside the VFC, a nonlinear feedback controller (NLFC) has been added, which is defined as a nonlinear function of the relative displacement and velocity $\psi(x_r, \dot{x}_r)$ and can be activated or deactivated using a switching device. Hence, the simulation results with and without the NLFC can be compared. The dynamics of the system described above can be expressed in a state space form as follow,

$$\begin{cases} \dot{\mathbf{y}} = \mathbf{A}(\mathbf{y})\mathbf{y} + \mathbf{B}_e f_e - \mathbf{B}_a(Bl)i_a \\ z = \mathbf{C}\mathbf{y} \end{cases} \tag{14}$$

where $\mathbf{y}$ is the state vector comprising the displacements and velocities of the structural and proof masses. $\mathbf{A}(\mathbf{y})$ is the system matrix, which includes the nonlinear model of the stiffness.

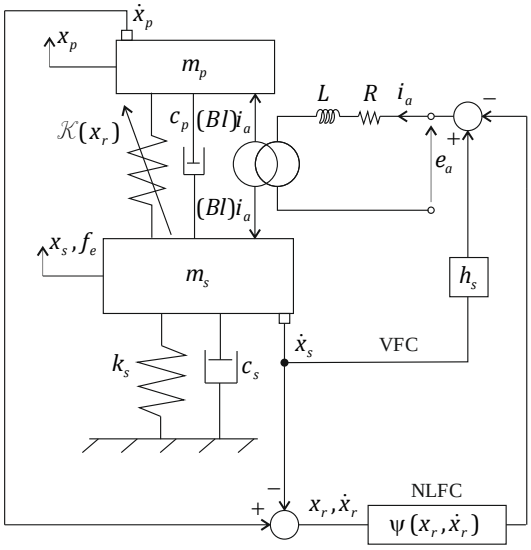

Figure 5. A lumped parameter model of the nonlinear actuator, structure, velocity feedback controller (VFC) and nonlinear feedback controller (NLFC).

$\mathbf{B}_e$ and $\mathbf{B}_a$ are the input matrices for the external and control forces, respectively. For the VFC loop, the output of the system z is defined as $z = \dot{x}_s$. Hence, for a fixed gain of the VFC, the input current to the actuator coil becomes,

$$i_a = h_s z \tag{15}$$

If the NLFC loop is also implemented, the output of the system becomes a vector defined as $\mathbf{z} = \{\dot{x}_s \quad \dot{x}_r\}^T$. The time series data are simulated using Simulink® ODE4 solver with fixed time-step sampled at 20 kHz. The parameters used in the simulations for the system shown in Figure 5 are reported in Table 1.

Table 1. Table of model parameters.

Property	m_s [kg]	k_s [N/m]	c_s [Ns/m]	m_p [kg]	k_p [N/m]	c_p [Ns/m]	Bl [N/A]	k_{sat} [N/m]	x_0 [mm]	ω_p [Hz]	ω_s [Hz]
Value	0.05	5000	0.32	0.032	100	1.4	1.6	$10^2 k_p$	1.25	8.9	50.3

Stability analysis

The stability of nonlinear systems can be evaluated using the describing function method [33, 34]. The nonlinear system can be represented using a feedback connection with the nonlinear element, as shown in Figure 6. As mentioned in the previous section, $K_{eq}(X_r)$ represents the DF of the nonlinear element, which is given by equation (11). $G(j\omega)$ instead comprises the remaining linear dynamics of the system, including the velocity feedback control with a constant gain h_s. Solving the system displayed in Figure 6 for the output variable x_r gives the following equation,

$$G(j\omega)K_{eq}(X_r) + 1 = 0 \tag{16}$$

which can be rewritten as,

$$G(j\omega) = -\frac{1}{K_{eq}(X_r)} \tag{17}$$

Figure 7 shows the polar plot of $G(j\omega)$ for different feedback gain h_s and the locus of the DF term. Being the nonlinearity an odd function, its DF takes only real values, hence $-1/K_{eq}(X_r)$ lies on the negative real axis. It should be noted that this term starts from $-1/k_p$ for $|X_r| < x_0$, then it goes towards the origin as $|X_r|$ increases.

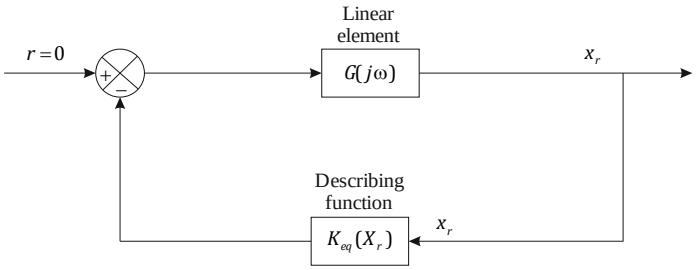

Figure 6. Block diagram in which the nonlinearity is represented as a feedback connection.

The intersection between the polar plot with the negative inverse of the describing function in Figure 7, hence the solution of equation (17), gives the condition for the existence of limit cycles in the nonlinear system [33, 34]. The amplitude of the limit cycle is given by the value of X_r corresponding to the negative inverse of the DF at the point of intersection. Similarly, the frequency of the limit cycle ω_{lc} corresponds to the value of the frequency of the polar plot at the point of the intersection [33, 34]. This procedure only gives a prediction of the existence of limit cycle, and due to its approximation nature, the results should be confirmed by time domain simulations. Figure 7 shows that higher control gains h_s cause the polar plot to intersect the negative inverse of the describing function at lower values. A simulation study has been carried out to understand how the feedback gain h_s affects the points of intersection. The result is shown in Figure 8(a) in terms of the amplitude of the limit cycle, which is the maximum relative displacement reached by the proof mass. For low values of h_s, a bigger relative displacement is needed to 'activate' the limit cycle than the one needed for higher values. However, for high values of the feedback gain, the curve is almost flat and it is settled at around 1.27 mm. Figure 8(b) shows the frequency of the limit cycle oscillations versus the velocity feedback gain. The frequency of the limit cycle increases as the feedback gain increases, but also in this case for high values of h_s the curve is almost flat at around 39.3 Hz. These results can be verified in time domain by analysing the impulse response of the system for increasing gains. Figure 9(a) shows the time series of the proof mass, structure and relative displacements, respectively, due to an impulse at time 0 with a magnitude of 10 N. The black solid line shows the response of the system without control. As the feedback gain is increased to 15 (blue dotted line), the response of the system to the same impulse shows that the vibration of the structural mass is significantly reduced, while the vibration of the proof mass is increased. However, the proof mass does not collide with the end stops. A further increase of the

feedback gain to the value of 18 (magenta dash-dotted line) causes the relative displacement to overshoot the allowed stroke length, hence an impulse like excitation is imparted to the structure. However, after two impacts this behaviour decays away.

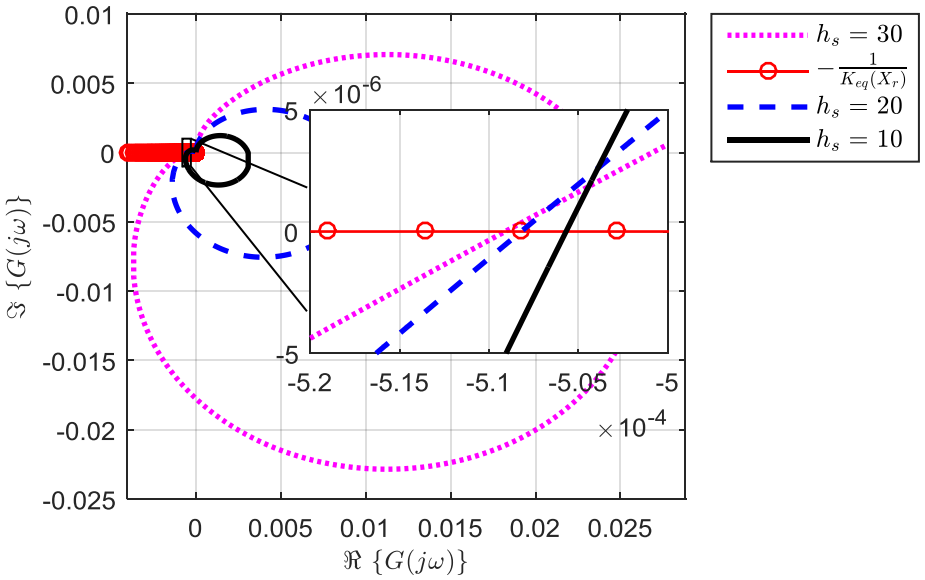

Figure 7. Polar plot of the FRF of the underlying linear system and the negative inverse DF for the detection of limit cycles.

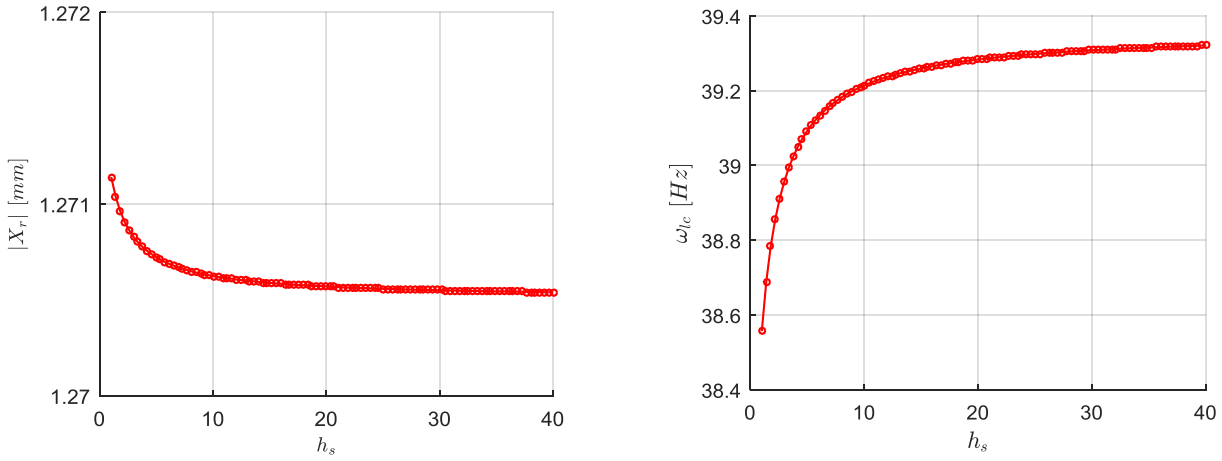

(a) (b)

Figure 8. (a) Amplitude of the limit cycles for several values of h_s; (b) Frequency of the limit cycles for several values of h_s.

Applying a slightly bigger feedback gain $h_s = 20$ (green dotted line) results in an unstable system. It should be noted that the feedback gain that causes the nonlinear system to go unstable ($h_{s,max} = 20$) is much lower than the one predicted with the linear analysis for the underlying linear model of the system ($h_{s,max} = 42$), as reported in [17, 35]. As the control system becomes unstable, limit cycle oscillations are observed, as shown in Figure 9(b). In this figure, the phase portrait of the relative coordinate is displayed for the same simulation conditions of Figure 9(a). It can be seen that an increase in the feedback gain rises the possibility of collisions with the end stops. From the time simulation shown in Figure 9(a,b) the amplitude and frequency of the limit cycle oscillation can be derived. In fact, the maximum amplitude of the relative displacement results to be 1.29 mm, which is slightly higher than the one predicted by the DF analysis. The frequency of the limit cycle can be calculated from the time series of Figure 9(a) considering the zero crossing of the signal. It follows that the frequency of the limit cycle is 27.6 Hz, which is lower than the 39.3 predicted by the DF analysis. These discrepancies in the outcomes have to be attributed to the contribution of the higher harmonics in the response that the DF tool does not take into account. However, the frequency of the limit cycle associated with the instability of the VFC is higher than the frequency of the instability for the underlying linear system, which is about the natural frequency of the actuator.

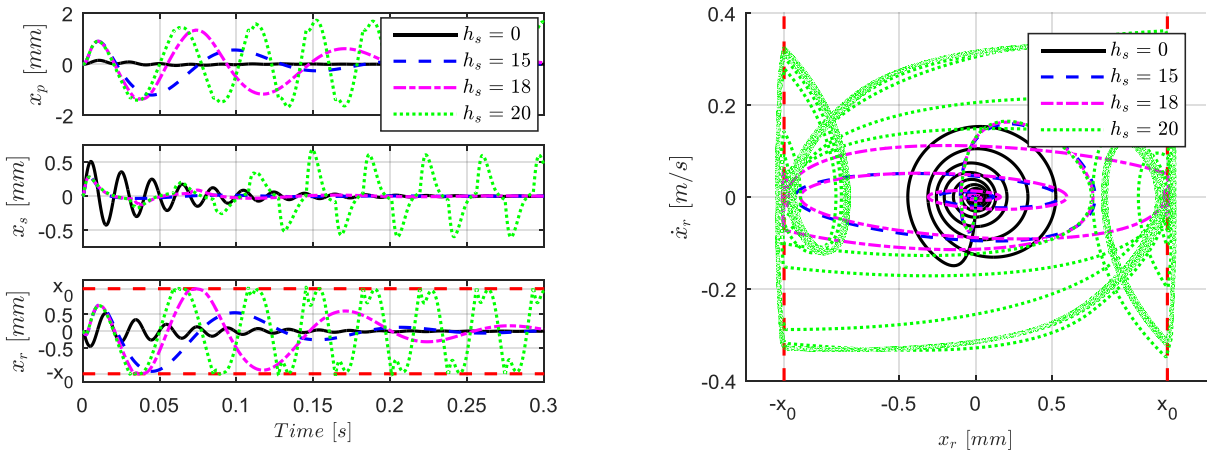

(a) (b)

Figure 9. (a) Time series of the response of the system to an initial impulse for several values of h_s; (b) phase portrait of the response of the system to an initial impulse for several values of h_s;

Nonlinear control results

The study of the previous section motivates for the development of a nonlinear controller, whose aim is to prevent the destabilisation of the feedback loop due to stroke saturation. The nonlinear feedback controller acts as a second loop alongside the VFC, as shown in Figure 5. We introduce the nonlinear feedback control law as,

$$\psi(x_r(t), \dot{x}_r(t)) = \frac{n_r \dot{x}_r(t)}{(x_0 - |x_r(t)|)^2} \tag{18}$$

where n_r is the feedback gain of the nonlinear controller. Equation (18) increases the damping of the inertial actuator as the proof mass approaches the end stops. A graphical representation of the control action is shown in Figure 10. It can be seen that for low values of the displacement the added control action is almost zero. As the displacement approaches the stroke limits, the nonlinear controller increases the active damping of the actuator. In such a configuration, the input current to the actuator's coil becomes,

$$i_a = h_s x_s - \frac{n_r \dot{x}_r}{(x_0 - |x_r|)^2} \tag{19}$$

Applying equation (19) can yield the current to take very large values with dangerous and impractical implications. Hence, a saturation limit on the maximum current has been set to $\pm 1\ A$.

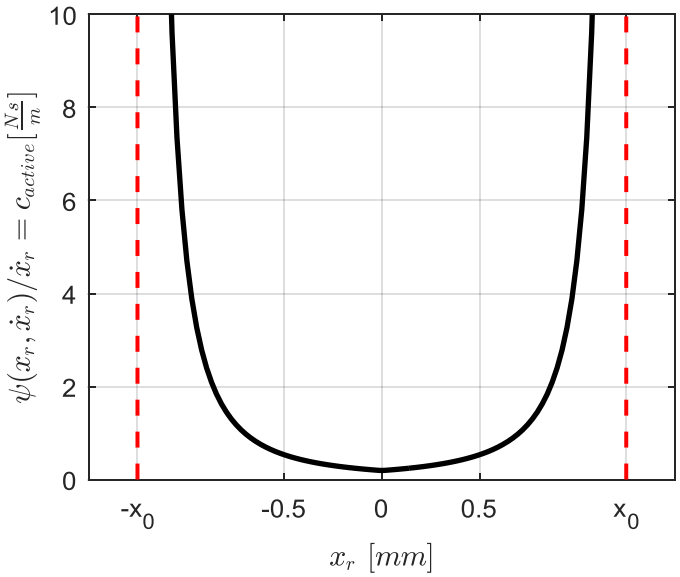

Figure 10. Control action of the proposed nonlinear controller.

Time simulation studies are carried out to asses the performance of the nonlinear controller. In particular a comparison with the simple velocity feedback control is made. Figure 11(a,b) shows the time histories and the phase portraits of the system with a feedback gain $h_s = 20$. In this scenario the system goes unstable if the NLFC is turned off. Implementing the NLFC described by equation (18) yields the proof mass to avoid the contact with the end stops, as the relative velocity goes to zero before the actuator saturates. Hence, the added NLFC loop increases the safe operating region of the inertial actuator.

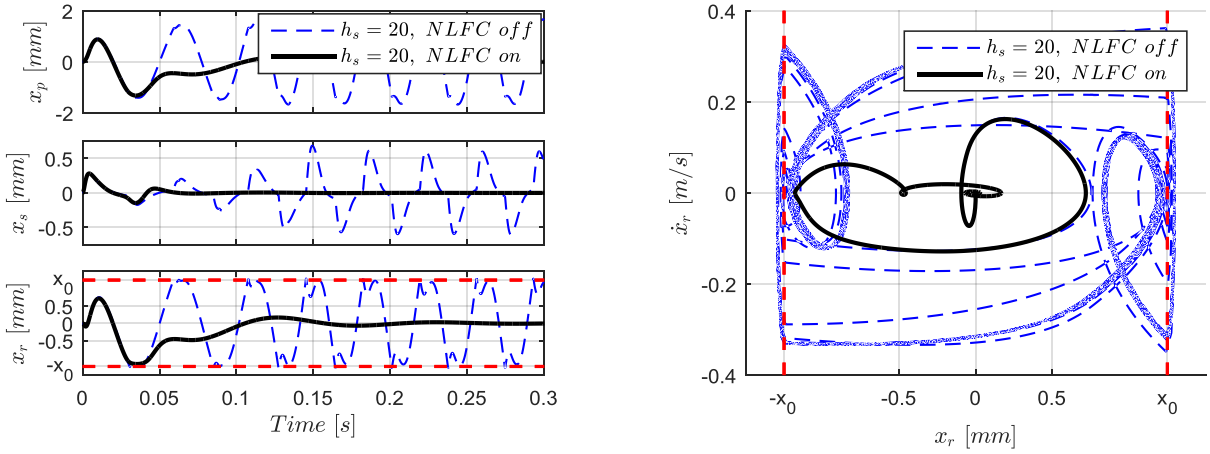

(a) (b)

Figure 11. Time history and phase portrait of the system ($h_s = 20$) with NLFC switched off and with NLFC switched on. (a) time histories; (b) phase portrait.

Conclusions

In this paper, a nonlinear feedback controller has been presented to avoid stroke saturation. Firstly, the mathematical model of the nonlinear inertial actuator has been derived, where the nonlinearity has been modelled by a piecewise linear stiffness. Simulation studies in frequency domain have been carried out using the harmonic balance method. It turned out that the nonlinear inertial actuator behaves significantly different compared to the underlying linear model. In particular, the resonance frequency of the inertial actuator increases as the amplitude of the excitation increases, due to the hardening nonlinearity. Secondly, the theoretical implementation of a stroke limited inertial actuator within a velocity feedback loop to control a single degree of freedom structure has been investigated. The stability for the nonlinear system operating in velocity feedback control has been analysed using both the describing function tool for the detection of limit cycles, and the time series and phase portrait analysis. It emerged that the maximum feedback gain that leads the nonlinear system to instability is consistently lower than the one predicted by the linear analysis, where the nonlinear element is neglected. This study is also confirmed by previous time simulation analysis [17]. The amplitude and frequency of the limit cycle oscillation have been calculated for both the frequency and time domain analysis. In particular, it has been shown that the frequency of the limit cycle associated with the instability of the VFC is higher than the frequency of the instability for the underlying linear system. This motivated the development of a nonlinear controller. A nonlinear feedback control law, which operates as a second loop alongside the classical velocity feedback, has been presented and analysed. Basically, the nonlinear controller increases the damping of the inertial actuator as the proof mass approaches the end stops, whereas it takes negligible values as the proof mass moves clear from the displacement constraints. Using time series and phase portrait analysis, it has been shown that the nonlinear feedback controller is able to increase the safe operating region of the actuator, without affecting the control performance. Hence, larger feedback gains can be used or larger impulse excitation can be withstood without leading the system to instability. Future work will be related on the experimental implementation of such nonlinear controller.

Acknowledgements

The authors gratefully acknowledge the European Commission for its support of the Marie Curie program through the ITN ANTARES project (General Agreement 606817). The results presented in this paper were partly obtained using the NI2D software developed by the Space Structures and Systems Laboratory (S3L), University of Liège.

References

[1] Meirovitch L. (1990) Dynamics and control of structures. John Wiley & Sons, New York.
[2] Fuller C. C., Elliott S. J., Nelson P. A. (1996) Active control of vibration. Academic Press.
[3] Elliott S. J. (2001) Signal processing for active control. Academic press.
[4] Inman D. J. (2006) Vibration with control. John Wiley & Sons.

[5] Fahy F., Gardonio P. (2007) Sound and structural vibration: radiation, transmission and response. 2nd ed., Elsevier Science.
[6] Wagg D. J., Neild S. A. (2010) Nonlinear vibration with control: for flexible and adaptive structures. Springer, the Netherlands.
[7] Preumont A. (2011) Vibration control of active structures: an introduction. Springer, the Netherlands.
[8] Gardonio P., Díaz C. G. (2010) Downscaling of proof mass electrodynamic actuators for decentralized velocity feedback control on a panel. *Smart Mater. Struct.* **19**.
[9] Rohlfing J., Gardonio P., Elliott S. J. (2011) Base impedance of velocity feedback control units with proof-mass electrodynamic actuators. *J. Sound Vib.* **330**:4661-4675.
[10] Rohlfing J., Elliott S. J., Gardonio P. (2012) Feedback compensator for control units with proof-mass electrodynamic actuators. *J. Sound Vib.* **331**:3437-3450.
[11] Díaz C. G., Paulitsch C., Gardonio P. (2008) Smart panel with active damping units. Implementation of decentralized control. *J. Acoust. Soc. Am.* **124**:898-910.
[12] Díaz C. G., Paulitsch C., Gardonio P. (2008) Active damping control unit using a small scale proof mass electrodynamic actuator. *J. Acoust. Soc. Am.* **124**:886-897.
[13] Paulitsch C., Gardonio P., Elliott S. J. (2006) Active vibration control using an inertial actuator with internal damping. *J. Acoust. Soc. Am.* **119**:2131-2140.
[14] Baumann O. N., Elliott S. J. (2007) The stability of decentralized multichannel velocity feedback controllers using inertial actuators. *J. Acoust. Soc. Am.* **121**:188-196.
[15] Paulitsch C., Gardonio P., Elliott S. J., Sas P., Boonen R. (2005) Design of a lightweight, electrodynamic, inertial actuator with integrated velocity sensor for active vibration control of a thin lightly-damped panel. *Proceedings of ISMA2004*, Leuven, Belgium, 239-253.
[16] Paulitsch C. (2005) Vibration control with electrodynamic actuators. *PhD Thesis*, ISVR, Southampton, UK.
[17] Baumann O. N., Elliott S. J. (2007) Destabilization of velocity feedback controllers with stroke limited inertial actuators. *J. Acoust. Soc. Am.* **121**:EL211-EL217.
[18] Zvonar G. A., Lindner D. K., Borojevic D. (1991) Nonlinear control of a proof-mass actuator to prevent stroke saturation. *Proceedings of the 8th VPI&SU Symposium*, Blacksburg, VA, USA, 37-48.
[19] Lindner D. K., Celano T. P., Ide E. N. (1991) Vibration suppression using a proofmass actuator operating in stroke/force saturation. *J. Vib. Acoust.* **113**:423-433.
[20] Lindner D. K., Zvonar G. A., Borojevic D. (1992) Limit cycle analysis of a nonlinear controller for a proof-mass actuator. *AIAA Dynamics Specialists Conference*, Dallas, TX, USA, 585-594.
[21] Lindner D. K., Zvonar G. A., Borojevic D. (1994) Performance and control of proof-mass actuators accounting for stroke saturation. *J. Guid. Control Dynam.* **17**:1103-1108.
[22] Lindner D. K., Zvonar G. A., Borojevic D. (1997) Nonlinear control of a proof-mass actuator. *J. Guid. Control Dynam.* **20**:464-470.
[23] Scruggs J., Lindner D. (1999) Optimal sizing of a proof-mass actuator. *40th Structures, Structural Dynamics, and Materials Conference*, St. Louis, MO, USA.
[24] Wilmshurst L. I. (2015) Analysis and control of nonlinear vibration in inertial actuators. *PhD Thesis*, ISVR, Southampton, UK.
[25] Dal Borgo M., Ghandchi Tehrani M., Elliott S. J. (2016) Dynamic analysis of nonlinear behaviour in inertial actuators. *Proceedings of MoViC2016 and RASD2016*, Southampton, UK, **744**:012027.
[26] Micromega Dynamics, http://www.micromega-dynamics.com/download/category/4-active-damping-device.html [Accessed: April 2017].
[27] Politansky H., Pilkey W. D. (1989) Suboptimal feedback vibration control of a beam with a proof-mass actuator. *J. Guid. Control Dynam.* **12**:691-697.
[28] Wilmshurst L. I., Ghandchi Tehrani M., Elliott S. J. (2013) Nonlinear vibrations of a stroke-saturated intertial actuator. *Proceedings of RASD2016*, Pisa, Italy.
[29] Wilmshurst L. I., Ghandchi Tehrani M., Elliott S. J. (2014) Nonlinear identification of proof-mass actuators accounting for stroke saturation. *Proceedings of ISMA2014*, Leuven, Belgium, 209-223.
[30] Detroux T., Renson L., Masset L., Kerschen G. (2015) The harmonic balance method for bifurcation analysis of large-scale nonlinear mechanical systems. *Comput. Meth. Appl. Mech. Eng.* **296**:18-38.
[31] Worden K., Tomlinson G. R. (2000) Nonlinearity in structural dynamics: detection, identification and modelling. Institute of Physics, Bristol, UK.
[32] Pavlov A., van de Wouw N., Nijmeijer H. (2006) Frequency response functions and Bode plots for nonlinear convergent systems. *Proceedings of the 45th IEEE Conference*, San Diego, CA, USA, 3765-3770.
[33] Slotine J.-J. E., Li W. (1991) Applied nonlinear control. Prentice-Hall, New Jersey, USA.
[34] Khalil H. K. (2002) Nonlinear systems. 3rd ed., Prentice-Hall, New Jersey, USA.
[35] Dal Borgo M., Ghandchi Tehrani M., Elliott S. J. (2016) Dynamic analysis of two nonlinear inertial actuators in active vibration control. *Proceedings of ISMA2016*, Leuven, Belgium, 1179-1192.